PAPER

Silicalite-1 zeolite encapsulated Cu–ZnO nanoparticles for selective CO_2 hydrogenation to oxygenates

Xu Wang, [iD] *[ab] Dongming Shen,[b] Hui Kang,[a] Kangzhou Wang, [iD] [c]
Chundong Zhang, [iD] *[d] Xinhua Gao, [iD] [e] Jianli Zhang, [iD] [e]
Eunjoo Jang*[f] and Jong Wook Bae [iD] *[b]

Selective conversion of CO_2 into value-added oxygenates, particularly methanol and dimethyl ether (DME), presents a promising route for CO_2 utilization. However, achieving both high selectivity and catalyst stability remained significant challenges. To address this, we report the fabrication of a core–shell-structured catalyst prepared by a steam-assisted crystallization (SAC) approach, in which highly dispersed Cu–ZnO nanoparticles (2.0–3.5 nm) are encapsulated within nanocrystalline silicalite-1 zeolite. The spatial confinement effects from silicalite-1 frameworks induce strong metal–zeolite interactions, effectively suppressing Cu–ZnO nanoparticle aggregation and sintering phenomena. This structural feature helps to preserve dominant populations of active Cu^+ species on thermally stabilized Cu–ZnO nanoparticles. As a result, the optimized catalyst enables efficient tandem conversion of CO_2 to oxygenates, achieving a CO_2 conversion of 21.5% with an oxygenate selectivity of 83.0% toward dimethyl ether (DME, 72.5%) and methanol (10.5%), where an optimized catalyst exhibits exceptional catalytic performance for the tandem CO_2-to-DME reaction. Comprehensive characterization reveals that the spatial confinement within the protective silicalite-1 matrix not only stabilizes highly dispersed Cu–ZnO nanoparticles and Cu^+ sites but also facilitates the formation and stabilization of key reaction intermediates. These synergistic effects are directly responsible for an enhanced catalytic activity, high DME selectivity, and prolonged operational durability observed during 300 h of continuous CO_2 hydrogenation.

1 Introduction

The urgent demand to decarbonize chemical manufacturing processes has positioned catalytic CO_2 hydrogenation as a critical technology for sustainable and valuable chemical

[a] *Institute for Advanced Study, Chengdu University, Chengdu 610106, China. E-mail: wangxu@cdu.edu.cn*

[b] *School of Chemical Engineering, Sungkyunkwan University (SKKU), 2066 Seoburo, Jangan-gu, Suwon, Gyeonggi-do 16419, Republic of Korea. E-mail: finejw@skku.edu*

[c] *School of Materials and New Energy, Ningxia University, Yinchuan 750021, Ningxia, China*

[d] *State Key Laboratory of Materials-Oriented Chemical Engineering, College of Chemical Engineering, Nanjing Tech University, Nanjing 211816, China. E-mail: zhangcd@njtech.edu.cn*

[e] *State Key Laboratory of High-Efficiency Utilization of Coal and Green Chemical Engineering, College of Chemistry & Chemical Engineering, Ningxia University, Yinchuan 750021, China*

[f] *SKKU Advanced Institute of Nanotechnology (SAINT), Sungkyunkwan University (SKKU), 2066 Seobu-ro, Jangan-gu, Suwon, Gyeonggi-do 16419, Republic of Korea. E-mail: ejjang1201@skku.edu*

production. The integration of renewable hydrogen production represents a cornerstone strategy for carbon emission reduction, enabling the conversion of CO_2 into value-added hydrocarbons and oxygenates.[1–4] Among these products, dimethyl ether (DME) and methanol are considered as the key platform intermediates, serving as both clean alternative fuels and versatile precursors for the production of olefins and aromatics.[5–7] Conventionally, the synthesis of methanol and DME proceeds *via* two successive reactions: syngas ($CO/CO_2/H_2$)-to-methanol process (STM), followed by separate methanol dehydration process (MTD: $2CH_3OH \leftrightarrow CH_3OCH_3 + H_2O$, $\Delta H_{298K} = -23.5$ kJ mol^{-1}).[5] In contrast, a direct CO_x-to-DME pathway combined with STM or CO_2-to-methanol (CTM) and MTD offers a compelling thermodynamic advantage by integrating both steps into a single reaction system with side reactions such as the exothermic water gas shift reaction (WGS) and endothermic reverse water gas shift reaction (RWGS). However, the direct process requires advanced bifunctional catalysts to overcome kinetic limitations and to suppress undesired competing

reactions such as the RWGS and hydrocarbon byproduct formation, which are prevalent in the CO_2 hydrogenation reaction.[6] Therefore, the efficient production of DME relies on bifunctional catalysis, where CO_x is hydrogenated to methanol over metal sites and the resulting methanol is successively dehydrated to DME over solid acidic sites. The synergy between two distinct catalytic functions, along with their structural compatibility and long-term stability, is critical for achieving high performance in a direct and durable CO_2-to-DME tandem reaction.

Cu–ZnO based catalytic systems remain the benchmark methanol synthesis catalysts due to their high activity and low preparation cost. However, they suffer from intrinsic limitations, including thermodynamically driven aggregation of Cu or Zn metal (oxides), which leads to gradual catalyst deactivation;[8–11] re-oxidation of active Cu species by water or CO_2;[12,13] and enhanced RWGS reaction activity to form CO, which significantly compromises methanol selectivity.[14–16] Therefore, stabilizing those active metal (oxide) sites within porous matrices is a promising strategy to prevent aggregation.[17] In particular, zeolitic frameworks offer unique advantages by combining crystalline microporosity, facilitating intermediate diffusion, and intrinsic acidity, supporting cascade reactions. However, the catalysts prepared using current encapsulation methods predominantly produce methanol, while DME formation is limited due to the presence of insufficient acidic sites for methanol dehydration.[18–24] Therefore, new synthetic approaches that incorporate tunable and abundant acidic sites into zeolite frameworks are essential for upgrading methanol to downstream DME and higher hydrocarbon products, as well as for enabling other extended tandem catalytic reactions that require multifunctional active sites.

Herein, we demonstrate a steam-assisted crystallization (SAC) approach (Scheme 1) to construct silicalite-1 encapsulated Cu–ZnO nanoparticles (2.0–3.5 nm) that enhance thermal-stability and introduce acidic functionalities in the tandem CO_2-to-DME catalytic reaction. This topotactic transformation from amorphous SiO_2 into crystalline zeolite enables homogeneous distribution of Cu–ZnO nanoparticles within the silicalite-1 frameworks, while also generating tunable Lewis acid sites through controlled crystallization time for 12–72 h. Systematic characterization confirms a near-complete amorphous-to-crystalline transition, the highest acid density modulation (1.682 mmol $g_{cat.}^{-1}$), and remarkable Cu^+ preservation in the CZ(0.9)@S-48 catalyst. As a result, this catalyst exhibits a high DME selectivity of 72.5% at 250 °C and excellent catalyst durability, maintaining the catalytic performance without any significant deactivation over 300 h continuous operation. These findings highlight the roles of silicalite-1 zeolitic confinement in stabilizing Cu^+ active sites, promoting the formate-mediated reaction pathway, and suppressing aggregation of Cu–ZnO nanoparticles and the RWGS side reaction by establishing a versatile strategy for designing cascade bifunctional catalysts.

2 Results and discussion

2.1 Structural properties of CZ(x)@S-t catalysts

The phase evolution and structural integrity of the CZ(x)@S-t catalysts were characterized through X-ray diffraction (XRD) analysis as well as high-resolution transmission electron microscopy (HRTEM), and the results are displayed in Fig. 1. The XRD patterns (Fig. 1a) reveal complete topological and morphological structural transformations of amorphous SiO_2 in CZ@Si into the well-defined silicalite-1 zeolite frameworks according to the MFI (PDF#21-1486) structure during the SAC step. The XRD patterns also show that the peak intensity gradually decreased with the extended crystallization time from 12 to 72 h, indicating the reduction in crystallinity and structural evolution. These changes are closely associated with variations in catalyst surface properties such as acidity, metal dispersion, and metal–zeolite interactions, which critically influence catalytic behaviors. Notably, no detectable diffraction peaks attributed to crystalline Cu or Zn metal (oxides) phases were observed based on the CuO (PDF#45-0973) and ZnO (PDF#44-0003) standard cards, implying that Cu–ZnO metal (oxides) nanoparticles are highly dispersed in the silicalite-1 crystallite shells with their small amounts less than 4 wt% on the fresh CZ(x)@S-t catalysts (Table S1).

The HRTEM analysis further reveals the structural evolution during the SAC step. Initially, the precursor material consists of amorphous SiO_2 nanospheres (~30 nm in size) encapsulating multi-core Cu–ZnO nanoparticles, as shown in Fig. 1b. With an extended crystallization duration from 12 to 72 h, these amorphous structures were transformed into hierarchically organized nanosized silicalite-1 zeolite with the size of ~200 nm, confining well-dispersed Cu–ZnO nanoparticles which aligns with our

Steam-assisted Crystallization (SAC)

SAC

Phase Transformation

CZ(x)@Si
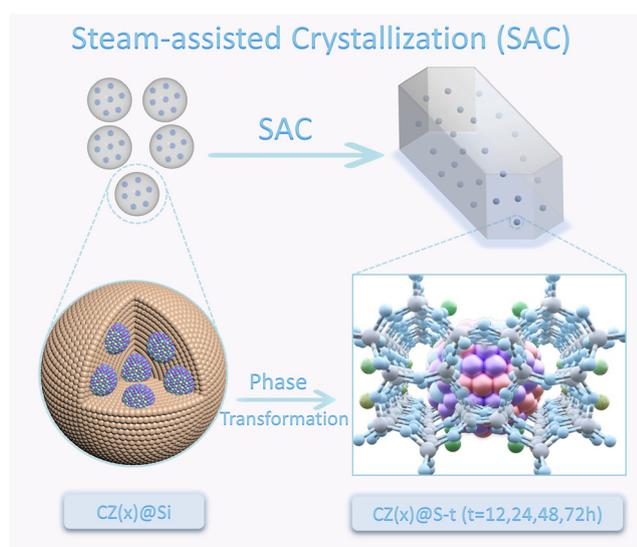
CZ(x)@S-t (t=12,24,48,72h)

Scheme 1 Schematic synthetic procedures of CZ(x)@S-t catalysts *via* the SAC method.
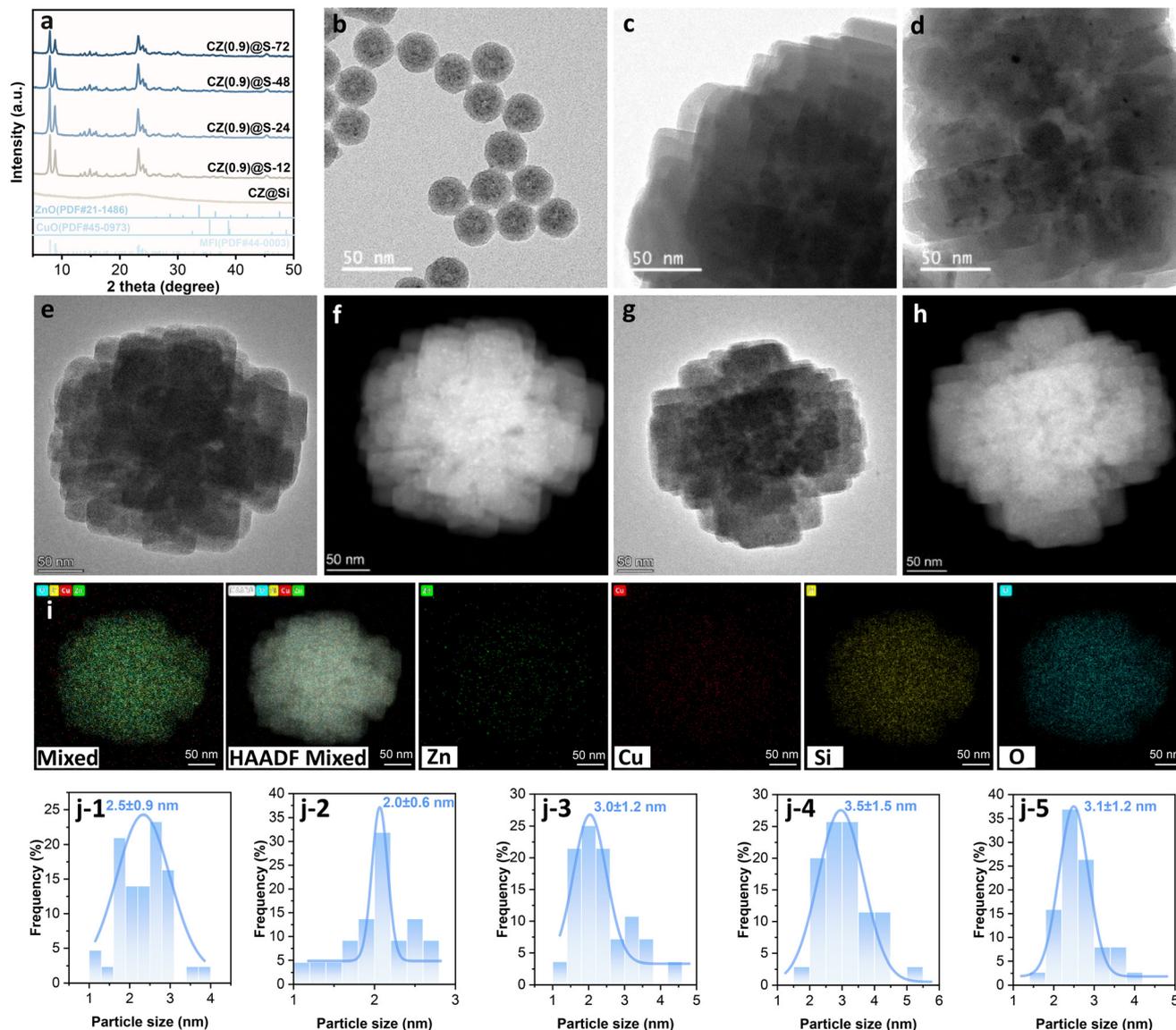
Fig. 1 XRD patterns of (a) CZ(0.9)@Si and CZ(0.9)@S-t (t = 12, 24, 48, 72); TEM images of (b) CZ@Si, (c) CZ(0.9)@S-12, (d) CZ(0.9)@S-24, and (e) CZ(0.9)@S-48; (f) HAADF images of CZ(0.9)@S-48 and (g) TEM image of CZ(0.9)@S-72; (h) HAADF image of the CZ(0.9)@S-72 catalyst; (i) EDS mapping of CZ(0.9)@S-48 and (j) particle size distribution of (1) CZ@Si, (2) CZ(0.9)@S-12, (3) CZ(0.9)@S-24, (4) CZ(0.9)@S-48, (5) CZ(0.9)@S-72.

previous work.[24] The spatial confinements are further validated by HRTEM-EDS elemental mapping images, which show homogeneous distribution of Cu and Zn species throughout the silicalite-1 frameworks as shown in Fig. 1i for CZ(0.9)@S-48, contributing to the formation of Lewis acid sites by reversibly forming Brönsted acid sites under a water environment for the methanol dehydration reaction.[25–27] In addition, statistical analysis of nanoparticle size distribution (Fig. 1j) indicates that CZ@Si exhibits Cu–ZnO nanoparticles with an average size of 2.5 nm (Fig. 1j-1), while those in the crystallized CZ(x)@S-t catalysts maintained a narrow size distribution in the range of 2.0–3.5 nm (Fig. 1j). Although slight variations in particle sizes are observed across the different crystallization durations, overall sizes were found to be within a narrow range, indicating that the zeolite

encapsulation effectively limits particle growth and aggregation throughout the SAC method. These spatial controls play key roles in maintaining the high dispersion of Cu–ZnO nanoparticles and preventing thermal sintering under the high-temperature reaction conditions, thereby enhancing long-term catalytic stability.

2.2 Surface properties of CZ(x)@S-t catalysts

The SAC process fundamentally alters the textural and surface properties of the CZ(x)@S-t catalysts. As shown in Fig. 2a and Table 1, the transformations of amorphous SiO$_2$ shells on CZ@Si into crystalline silicalite-1 frameworks led to significant increases in surface areas from 101 to ~300 m^2 g^{-1} by forming intraparticular mesopores as revealed by
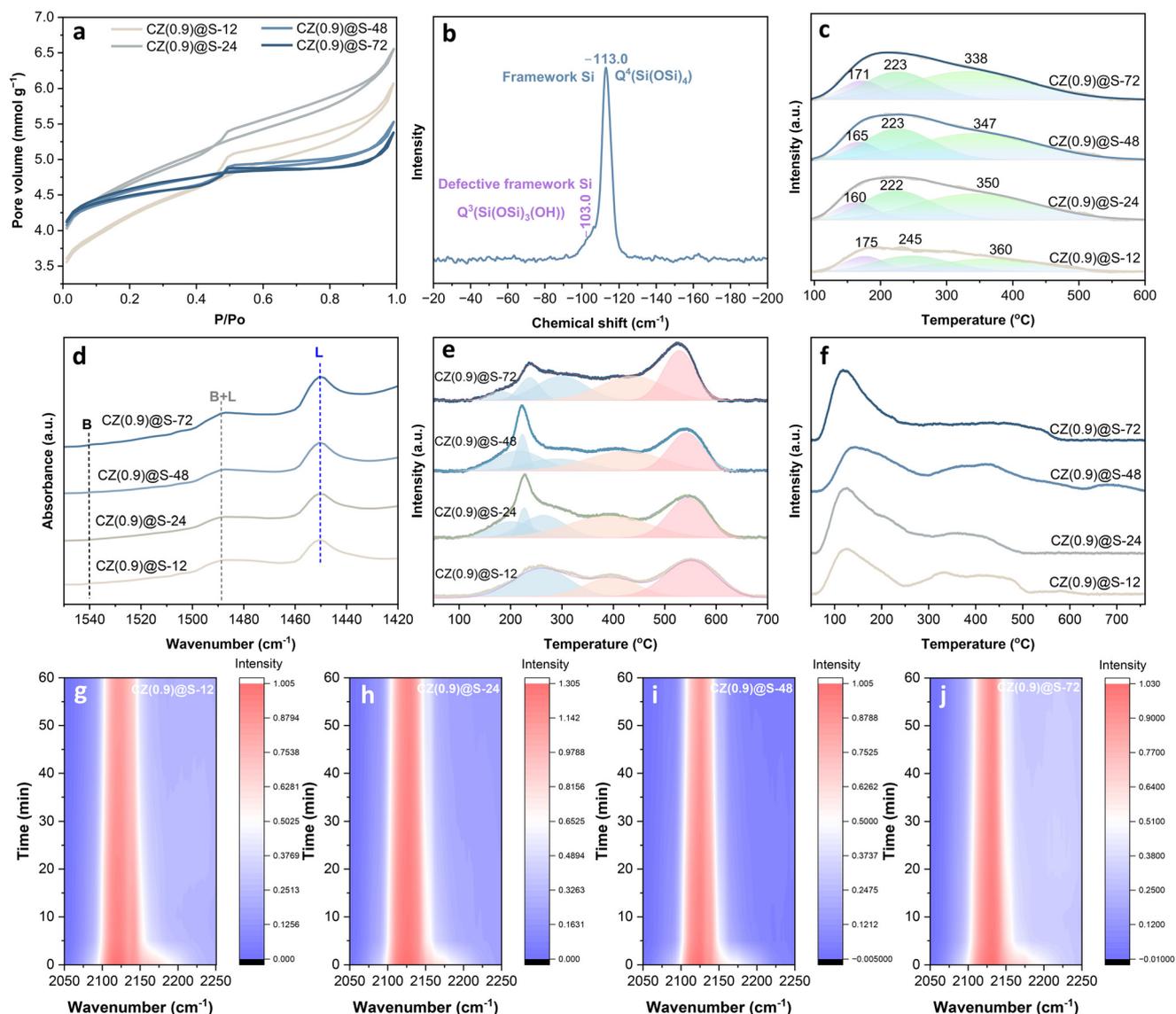
Fig. 2 Structural and surface properties of (a) N_2-sorption of CZ(0.9)@S-t catalysts, (b) ^{29}Si NMR spectra of CZ(0.9)@S-48, (c) NH_3-TPD patterns, (d) Py-FTIR peaks, (e) H_2-TPR profiles, (f) CO_2-TPD profiles and (g–j) *in situ* CO-DRIFTS patterns of the CZ(0.9)@S-t catalysts.

pore size distribution in Fig. S1. These structural transitions, involving the reorganization of amorphous SiO_2 into a tetrahedral SiO_4^{4-} unit, reflect the inherent microporous architectures of MFI-type silicalite-1, which features well-defined networks of 10-membered ring (10-MR) channels with micropore sizes of 5.1 × 5.5 Å and 5.3 × 5.6 Å.[28] The resulting hierarchical porosity enhances mass transport properties, and those structural reorganizations are further confirmed by ^{29}Si MAS NMR spectroscopy analysis (Fig. 2b), which shows sharp and distinct peaks at −113 ppm (Q^4, Si(OSi)$_4$) and −103 ppm (Q^3, Si(OSi)$_3$OH).[29,30] The high Q^4/Q^3 ratio observed in CZ(0.9)@S-48 indicates highly condensed MFI frameworks, confirming nearly complete crystallization of the amorphous SiO_2 shells on the CZ@Si.

NH$_3$-TPD profiles (Fig. 2c and S2) further elucidated the evolution of surface acidity on the CZ(x)@S-t catalysts with

varying crystallization duration (12–72 h). Three distinct desorption regions were identified, corresponding to weak acidic sites (100–200 °C), medium-strength acidic sites (200–300 °C), and strong acidic sites (>300 °C). Quantitative analysis as summarized in Tables 1 and S2 (summary of three successive analyses) demonstrated that total acidity increased with an increase in crystallization duration, reaching up to 1.682 mmol $g_{cat.}^{-1}$ on CZ(0.9)@S-48. This observation suggests the acidic site balance between zeolite crystallinity and preservation of Cu and Zn nanoparticles, both of which contribute to the formation of acidic sites.[25–27] Prolonged crystallization beyond 48 h slightly decreased total acidity (1.552 mmol $g_{cat.}^{-1}$) as confirmed on CZ(0.9)@S-72 with a lower crystallization degree as confirmed by the smaller XRD peak intensity in Fig. 1a. Pyridine-adsorbed FTIR analysis on the CZ(0.9)@S-t catalysts (Fig. 2d) confirms that the acidity

Table 1 Characteristics of the hybridized CZ(x)@S-t catalysts with their catalytic performances

Catalyst	N$_2$-sorption[a] $S_g/P_V/P_D$	H$_2$ consumption (mmol g$_{cat.}^{-1}$) (L/M/H (total))[b]	CO$_2$-TPD (mmol g$_{cat.}^{-1}$) (W/M/S (total))[c]	NH$_3$-TPD (mmol g$_{cat.}^{-1}$) (W/M/S (total))[d]	Catalytic activity (mol%)[e] Conversion (CO$_2$)	Selectivity (CO/CH$_4$/methanol/DME)
CZ@Si	101/0.58/29.0	—	—	—	14.9	21.4/4.3/74.3/0
CZ(0.9)@S-12	334/0.21/3.6	0.168/0.114/0.228 (0.510)	0.290/0.117/0.089 (0.496)	0.183/0.316/0.341 (0.840)	21.3	11.3/4.3/79.3/9.4
CZ(0.9)@S-24	328/0.12/3.9	0.213/0.200/0.190 (0.603)	0.481/0.186/0.035 (0.702)	0.200/0.550/0.768 (1.518)	19.4	19.4/0/25.6/55.0
CZ(0.9)@S-48	310/0.06/4.2	0.244/0.181/0.176 (0.601)	0.331/0.162/0.141 (0.634)	0.212/0.614/0.856 (1.682)	21.5	17.0/0/10.5/72.5
CZ(0.9)@S-72	311/0.05/4.2	0.208/0.176/0.191 (0.575)	0.358/0.161/0.099 (0.618)	0.219/0.590/0.743 (1.552)	19.7	12.7/0/15.6/71.7
Cu@S-48	311/0.08/3.3	0.200/0.145/0.124 (0.469)	0.197/0.160/0.148 (0.505)	0.183/0.602/0.224 (1.009)	16.7	37.7/1.0/14.9/46.4
CZ(0.4)@S-48	273/0.05/3.2	0.173/0.110/0.041 (0.324)	0.208/0.201/0.072 (0.481)	0.439/0.440/0.665 (1.544)	19.1	17.0/1.9/49.9/31.3

[a] Summarized N$_2$-sorption results of BET surface area (S_g, m^2 g^{-1}), pore volume (P_V, cm^3 g^{-1}), average pore diameter (P_D, nm). [b] Amount of H$_2$ consumption (mmol g$_{cat.}^{-1}$) was estimated by H$_2$-TPR analysis with three different reduction peaks at lower temperature:150–300 °C (L), medium temperature: 300–500 °C (M) and high temperature >500 °C (H). [c] Amount of desorbed CO$_2$ (mmol g$_{cat.}^{-1}$) was calculated according to different desorption temperatures of CO$_2$ such as weak (W) at 100–200 °C, medium (M) at 200–400 °C and strong (S) basic sites at >400 °C. [d] Acidic sites measured by NH$_3$-TPD analysis and categorized with as (W), medium (M) and strong (S) acid sites with their total amount (average values for 3 successive analysis) at maximum desorption of NH$_3$ in temperature ranges of 100–200, 200–300 and >300 °C, respectively. [e] Catalytic activity of CZ(x)@S-t catalysts was measured under the reaction conditions of T = 250 °C, P = 5.0 MPa, H$_2$/CO$_2$ molar ratio of 3/1 (4.0 vol% N$_2$ balanced) with a space velocity (SV) of 3000 mL g$_{cat.}^{-1}$ h^{-1} after the reduction treatment at 300 °C for 2 h with 5 vol% H$_2$ (N$_2$ balanced).

predominantly originated from Lewis acid sites. Characteristic bands at 1445–1460 cm^{-1}, indicative of pyridine molecules coordinated to Lewis acid sites,[26] were observed, whereas bands associated with Brønsted acid sites (~1540 cm^{-1}) were not clearly observed.[31] These observations imply that the acid functionality arises primarily from the coordinatively unsaturated framework Si atoms or extra-framework Zn and Cu species.[25–27] The prevalence of Lewis acid sites by reversibly forming Brønsted acid sites due to water formed during reaction is highly beneficial for methanol dehydration,[32,33] which increases the bifunctional catalyst's activity for direct CO$_2$-to-DME conversion due to an increased synergistic contribution between CTM and successive MTD reaction with an increased methanol conversion as well.

H$_2$-TPR analysis (Fig. 2e and S3) elucidates important insights into Cu oxidation states or metal–zeolite interactions. Three distinct reduction domains were identified low-temperature peaks (<300 °C), which could be assigned to the possible reduction of surface Cu^{2+} to Cu$^+$ or one step Cu^{2+} to Cu^0 species,[34,35] mid-temperature peaks in the range of 300–500 °C, corresponding to the stepwise reduction of Cu^{2+} to Cu$^+$ in strongly interacting environments and high-temperature peaks (>500 °C) could be attributed to the reduction of ion-exchanged Cu$^+$ species in zeolite to metallic Cu^0 species.[35,36] These results suggest that the Cu$^+$ phases are the dominant species remaining after the reduction pretreatment (300 °C) prior to the CO$_2$ hydrogenation reaction over CZ(0.9)@S-t catalysts, owing to stronger interactions between Cu and zeolite frameworks induced by spatial confinements. Additionally, it was found that the presence of ZnO in the catalysts further inhibits the reduction of Cu species compared to the Zn-free Cu@S-48 as shown in Fig. S3. This observation indicates that ZnO addition promotes the preservation of partially reduced Cu species under reduction conditions (300 °C), which favors the stabilization of active copper sites as well. Moreover, the Zn species was highly dispersed in the entire crystallites according to the TEM-EDS mapping images as shown in Fig. 1i, suggesting that the encapsulation of the Zn promoter in silicalite-1 zeolite not only forms Cu–ZnO interfacial sites for methanol formation,[8,9] but also contributes to the possible formation of Lewis acid sites for methanol dehydration to DME,[32,33] which confirms the significance of Zn species in CZ(x)@S-t for catalytic performances of CO$_2$ hydrogenation to oxygenates.

Fig. 2f and Table 1 present CO$_2$-TPD profiles and corresponding amounts of CO$_2$ desorption on the CZ(x)@S-t catalysts. Three desorption peaks are evident, corresponding to weak (W), medium (M), and strong (S) basic sites.[37] The peaks at the lowest temperatures (<200 °C) are assigned to weak basic sites originating from surface OH groups, while medium-strength basic sites, desorbing at intermediate temperatures, are attributed to linearly adsorbed O–C–O species on metal–oxygen pairs such as Zn–O species.[38] The high-temperature peaks (>500 °C), indicative of strong basic sites, are attributed to the bridge-bonded M–O–C–O–M species associated with surface O^{2-} anions.[39] Notably, the total amount of desorbed CO$_2$ was increased with an increase in crystallization duration from 12 to 24 h (from 0.496 mmol g^{-1} on CZ(0.9)@S-12 to 0.702 mmol g^{-1} on CZ(0.9)@S-24) and decreased again to 0.618 mmol g^{-1} on CZ(0.9)@S-72, while the decreased Cu/Zn ratio on CZ(0.4)@Si-48 showed a slightly smaller amount of desorbed CO$_2$ molecules with 0.482 mmol g^{-1} resulting in a slightly lower CO$_2$ conversion as well. This reduction in CO$_2$ adsorption capacity on the CZ(x)@S-t catalysts was attributed to the strong interactions involving oxygen vacant sites. The loss of CO$_2$ adsorption sites with prolonged crystallization duration likely contributes to the suppression of CO$_2$ conversion due to the depletion of oxygen vacant sites, potentially caused by leaching of CuO species during the SAC process. Furthermore, *in situ* CO-DRIFTS

(Fig. 2g and h) provides the direct evidence of Cu^+ preservation even after its reduction at 300 °C for 2 h. The persistent band at 2130 cm^{-1}, assigned to the $v(CO)$ stretch mode of Cu^+–CO carbonyls,[39–42] remains intense even after 60 minutes of N_2 purging (Fig. 2g–j). The stabilized Cu^+ species seem to create better structural configurations for CO_2 activation, while Lewis acid sites synergistically promote methanol dehydration, enabling efficient cascade catalysis toward DME formation.

2.3 CO_2 hydrogenation activity to DME and methanol over CZ(*x*)@S-*t* catalysts

The catalytic performances of the synthesized CZ(*x*)@S-*t* catalysts for CO_2 hydrogenation to DME and methanol were systematically evaluated in a fixed-bed tubular reactor under the reaction conditions of P = 5.0 MPa, T = 250 °C, space velocity (SV) = 3000 mL $g_{cat.}^{-1}$ h^{-1}. Fig. 3 and S4–S6 comprehensively document structure–activity relationships
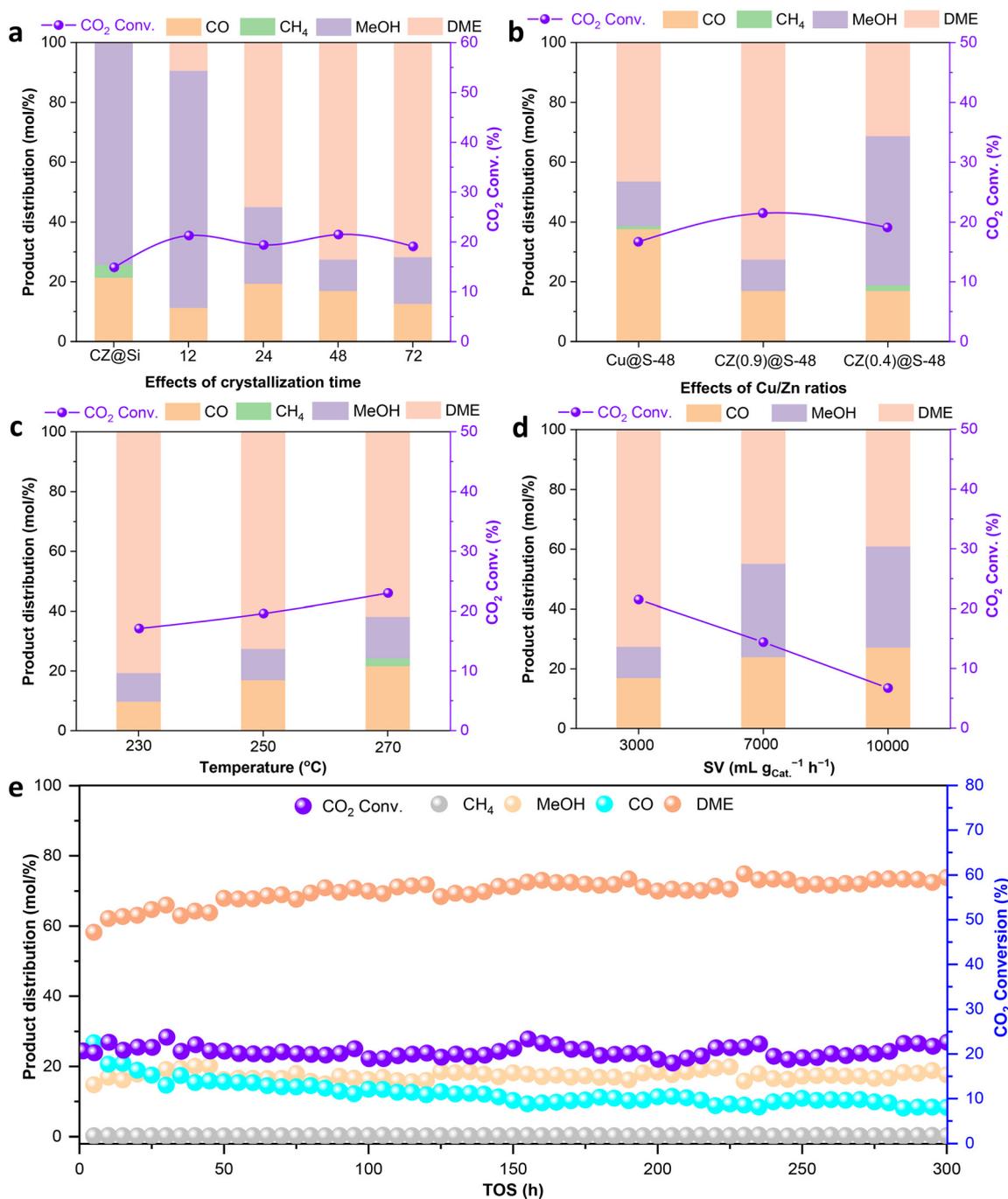

Fig. 3 Catalytic performances of CZ(*x*)@S-*t* catalysts with effects of (a) crystallization time, (b) Cu/Zn molar ratio, (c) reaction temperature from 230 to 270 °C, (d) space velocity (SV) and (e) long-term catalyst stability for 300 h reaction.

Industrial Chemistry & Materials

across the catalyst series with varied crystallization duration (t = 12–72 h) and Cu/Zn molar ratio. As shown in Fig. 3a and Table 1, the parent CZ@Si exhibits limited catalytic activity, achieving only 14.9% CO_2 conversion with 74.3% methanol selectivity without DME formation, consistent with its lack of acidic sites for methanol dehydration. As expected, the CZ(0.9)@S-t catalysts obtained *via* progressive SAC treatment gradually developed acidic sites that enabled further methanol dehydration to DME. Specifically, CZ(0.9)@S-12 achieved a higher CO_2 conversion of 21.3% with 79.3% methanol and 9.2% DME selectivity (11.3% of CO), demonstrating the initial emergence of bifunctional synergy

by facilitating the diffusion of *in situ* formed methanol to Lewis acid sites. The catalytic performance over CZ(0.9)@S-48 emerged at the highest acidity (1.682 mmol $g_{cat.}^{-1}$, Table 1), enabling nearly complete methanol dehydration ($2CH_3OH \leftrightarrow CH_3OCH_3 + H_2O$). This resulted in a high DME selectivity of 72.5% and a decreased methanol selectivity of 10.5%, indicating the kinetic dominance of the dehydration step. In contrast, the excessive crystallization duration on CZ(0.9)@S-72 led to the decreased DME selectivity of 71.7%, attributed to the diminished acidic sites (1.552 mmol $g_{cat.}^{-1}$). The balance between sufficient active sites for CO_2 hydrogenation to methanol and methanol dehydration to DME over the Cu–
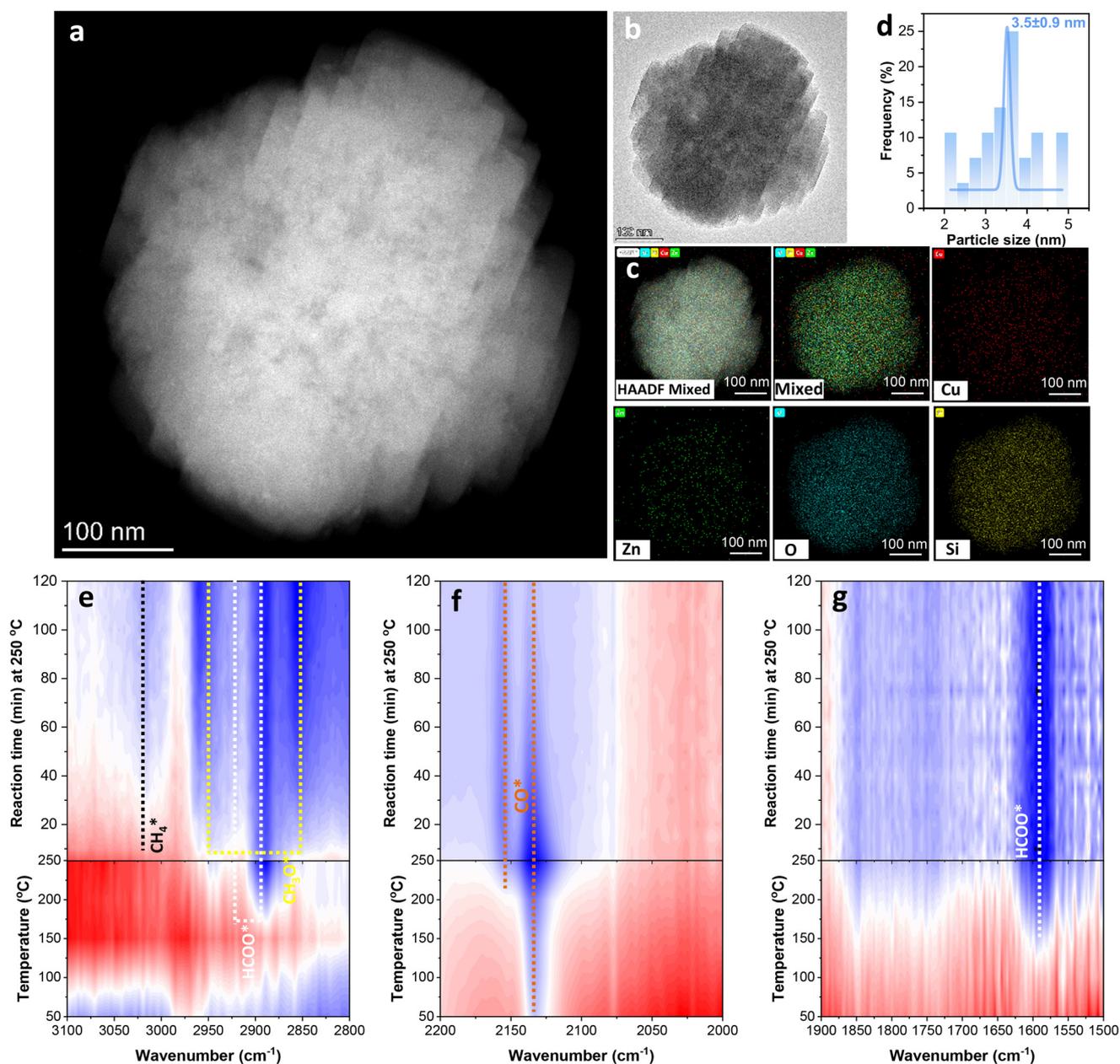

Fig. 4 (a–c) HRTEM and EDS mapping images of the used CZ(0.9)@S-48 after 300 h reaction; (d) particle size distribution and (e–g) *in situ* DRIFTS analysis results of CZ(0.9)@S-48 under the reaction conditions of T = 250 °C, P = 2.0 MPa, H_2/CO_2 molar ratio of 3.

ZnO nanoparticles and Lewis acidic sites are found to be crucial for the selective conversion of CO_2 into DME and methanol oxygenates. In addition, it is revealed in Fig. 3b that the best Cu/Zn molar ratio is 0.9 (Table S1), and Zn promotion significantly suppressed CO formation *via* the RWGS reaction, as evidenced by the higher CO selectivity on Zn-free Cu@S-48 (37.7%). Operational parameter studies (Fig. 3c and d) demonstrate inherent trade-offs between catalytic activity and oxygenate selectivity to DME and methanol. At the reaction temperature of 230 °C, CO_2 conversion was kinetically limited to 17.1%, yet oxygenate selectivity (DME and methanol) reached up to 87.5%. At 270 °C, the thermodynamically favored RWGS reaction led to a high CO selectivity of 29.3% and a drop in DME selectivity to 63.8%. A lower space velocity (SV = 3000 mL $g_{cat.}^{-1}$ h^{-1}) resulted in prolonged residence of reactants, facilitating consecutive methanol-to-DME conversion (DME selectivity of 72.5%). Conversely, a higher SV (up to 10 000 mL $g_{cat.}^{-1}$ h^{-1}) led to an increased methanol selectivity (33.8%), decreased DME selectivity (39.0%), and lowered CO_2 conversion (6.7%), likely due to an insufficient contact with active sites.

CZ(0.9)@S-48 demonstrated an excellent stability over 300 h of longevity test (Fig. 3e), maintaining CO_2 conversion at ~20% and DME selectivity above 70.1%. HRTEM analysis (Fig. 4a–c) on the used CZ(0.9)@S-48 after 300 h confirms that the Cu and Zn species were still highly dispersed (Fig. 4e) with minimized aggregation and maintained promotional Zn effects which preserved more active Cu–ZnO interfaces for methanol formation; also the Cu–ZnO nanoparticles maintained well-dispersed states with an average size of 3.5 ± 0.9 nm (Fig. 4d), comparable to the initial size of 3.5 ± 1.5 nm with no detectable sintering phenomena. This also validates the spatial confinement effects of silicalite-1 shells in preserving catalyst morphology and catalytic performance. Elemental mapping analysis confirmed the high dispersion of Cu and Zn metal (oxides), which may contribute to maintaining active Lewis acid sites for methanol dehydration. This remarkable stability originates from the spatial confinement of Cu–ZnO nanoparticles in silicalite-1 frameworks, which effectively prevents aggregation and preserves the initial activity and selectivity during CO_2 hydrogenation. In comparison, the present studies for encapsulated Cu-based catalysts (Table S3) reveal that the absence of abundant acidic sites will only generate the methanol product, suggesting that the controlled Lewis acid sites on the CZ(x)@S-t catalysts are efficient ways for the direct CO_2-to-DME tandem reaction.

2.4 *In situ* DRIFTS analysis and proposed reaction mechanisms

In situ diffuse reflectance infrared Fourier transform spectroscopy (DRIFTS) was conducted at an elevated pressure of 2.0 MPa and reaction temperature of 250 °C by using the CZ(0.9)@S-48 catalyst (Fig. 4e–g) and the CZ(0.9)@S-12 (Fig. S7) catalyst, respectively, which were *in situ* reduced at 300 °C

for 1 h. Temperature-programmed and time-resolved spectra are acquired with 4 cm^{-1} resolution, capturing the dynamic evolution of surface intermediates during CO_2 hydrogenation. In particular, the critical vibrational signatures revealed a cascade of surface reactions occurring at different reaction temperatures. It was found in Fig. 4f that the emergence of characteristic bands at 2155 and 2130 cm^{-1} confirmed the absorbed CO* species on Cu^+ sites,[41,43–45] or the formed gas-phase CO product during the CO_2 hydrogenation. The immediate appearance of these bands at 50 °C indicates facile dissociative adsorption of CO_2 upon its introduction into the DRIFT cell. Meanwhile, as reaction time increased at the reaction temperature of 200 to 250 °C, the bands at 2939, 2887, and 1580 cm^{-1}, assigned to the formation of formate species,[46–49] gradually intensified, indicating that higher reaction temperatures promote the hydrogenation of activated CO_2 species. The subsequent generation of methoxy or methanol species, indicated by the bands at 2960 and 2855 cm^{-1},[50,51] supports the formate-pathway that transforms CO_2 into methanol and subsequent dehydration to DME product over the CZ(x)@S-t catalysts. Notably, methoxy formation lagged behind formate appearance by ~20 minutes, suggesting that the formate hydrogenation seems to be a rate-determining step (RDS) for methanol synthesis.[52,53] Besides, it was observed (Fig. S7) that the major intermediate species on the CZ(0.9)@S-12 catalyst were formate (2939, 2887, 1580 cm^{-1}), methoxy (2960, 2855 cm^{-1}), CO (2155, 2133 cm^{-1}) and methane (3016 cm^{-1}) which appeared at similar wavenumber. In comparison, the peak intensity on CZ(0.9)@S-12 for formate species was much smaller and for methoxy higher, which indicates that the methanol formation over CZ(0.9)@S-12 is dominant *via* the hydrogenation of formate, while the peak intensity of methoxy species was found to be lower on CZ(0.9)@S-48, which also suggests its fast consumption to generate DME species *via* the dehydration reaction.

The proposed mechanism is described in Fig. 5, showing that CO_2 molecules are initially activated and hydrogenated to formate species over Cu^+ sites, followed by hydrogenation to form methanol. Finally, the formed-methanol is subsequently dehydrated into DME on the Lewis acid sites (or Brønsted acid sites generated by its hydration with water) in the silicalite-1 frameworks. Based on *in situ* DRIFTS analysis, the mechanisms for the tandem conversion of CO_2 to DME are schematically presented in Fig. 5. Initially, CO_2 and H_2 reactants are dissociated on the active Cu–ZnO surfaces, facilitating the formation of formate intermediates and their subsequent hydrogenation into surface methoxy species on the surfaces of metal oxides and zeolites. Dehydration of these methoxy species from methanol occurs on the Lewis acidic sites of the silicalite-1 surfaces to yield DME and methanol as final products. This enhanced catalytic performance on the CZ(0.9)@S-48 catalyst is attributed to the synergistic combination of multiple structural and chemical features within core–shell-structured architectures including thermally stable Cu–ZnO nanoparticles encapsulated by
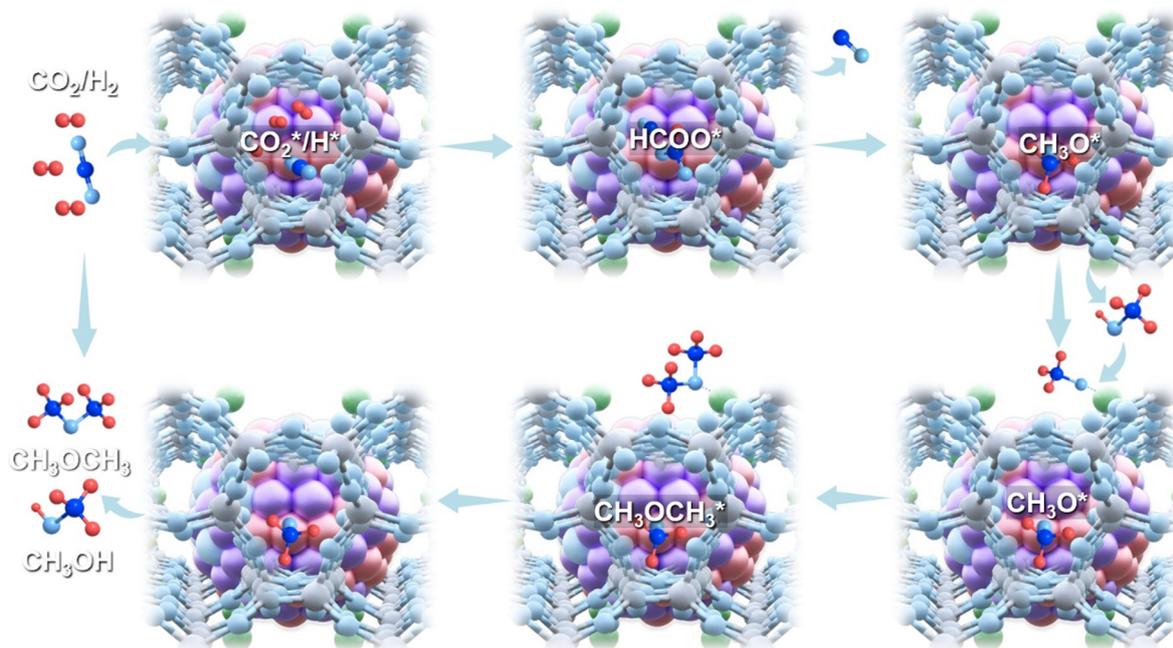
Fig. 5 Proposed reaction mechanisms for CO_2 hydrogenation to dimethyl ether (DME) and methanol over CZ(x)@S-t catalysts.

silicalite-1 overlayers, exhibiting high crystallinity, abundant Lewis acid and basic sites, and a large population of active Cu^+ species. These factors collectively contribute to an enhanced activity, long-term stability, and efficient mass transfer, enabling effective tandem conversion of CO_2 to oxygenates on the core–shell structured bifunctional catalyst.

3 Conclusions

In summary, the highly dispersed Cu–ZnO nanoparticles with sizes of 2.0–3.5 nm were successfully encapsulated within the nanocrystalline silicalite-1 zeolite frameworks *via* the SAC approach. Under optimized conditions (Cu/Zn ratio of 0.9, crystallization time of 48 h), strong metal–zeolite interactions effectively suppressed aggregation of Cu–ZnO nanoparticles and preserved dominant populations of active Cu^+ species. The resulting bifunctional catalyst demonstrated an excellent catalytic performance for tandem hydrogenation of CO_2 to methanol and its subsequent dehydration to DME, achieving a CO_2 conversion of 21.5% and combined oxygenate selectivity of 83.0% including 72.5% DME. The enhanced catalytic activity and stability were attributed to the synergistic effects of the spatial confinement by silicalite-1 with abundant Lewis acidic sites, which not only stabilizes Cu^+ sites but also facilitates the DME formation in an efficient cascade catalytic reaction. Overall, this study presents a robust and generalized approach for the preparation of heterogeneous catalysts to design thermally stable bifunctional catalysts with tunable acidity, suitable for other extended tandem catalysis reactions requiring multifunctional active centers.

4 Experimental section

4.1 Preparation of CuZnO@SiO$_2$ and CuZnO@silicalite-1

Cu–ZnO@silicalite-1 catalysts were prepared *via* a two-step strategy including the synthesis of Cu–ZnO@SiO$_2$ through a well-known reverse micelle method and the following synthesis of Cu–ZnO@silicalite-1 *via* a steam-assisted crystallization (SAC) approach by using the as-synthesized Cu–ZnO@SiO$_2$ nanoparticles (CZ@Si). For more details, SiO$_2$-encapsulated Cu–ZnO nanoparticles with different Cu/Zn molar ratios (denoted as Cu@Si, CZ(0.9)@Si and CZ(0.4)@Si) were prepared according to our previous work.[24] In detail, the CZ(x)@SiO$_2$ (x = 0.4 and 0.9) and Zn-free CuO@SiO$_2$ catalysts with a different Cu/Zn molar ratio of x were prepared by dissolving the metal precursors of Cu(NO$_3$)$_2$·3H$_2$O and Zn(NO$_3$)$_2$·6H$_2$O, which were previously dissolved in 5 mL deionized water (DIW), and 10.5 g Brij-C10 (polyethylene glycol hexadecyl ether) as a non-ionic surfactant was dissolved in 50 mL cyclohexane at 50 °C. The metal precursor solution was slowly dropped into Brij-C10 solution under stirring conditions over 1 h. Successively, aqueous ammonium hydroxide (3 mL) and tetraethyl orthosilicate (TEOS, 5 mL) were dropped into this solution under vigorous stirring conditions over 2 h to obtain a blue-colored solution. The resulting powders of CZ(x)@SiO$_2$ and CuO@SiO$_2$ were collected after centrifugation by using 30 mL ethanol solvent and dried at 80 °C overnight and eventually calcined at 550 °C for 2 h at a ramp rate of 1 °C min^{-1}.

The core–shell-structured Cu–ZnO@silicalite-1 catalysts, encapsulated with silicalite-1 on the Cu–ZnO nanoparticles, were prepared by controlling the crystallization duration (t) for 12, 24, 48 and 72 h with varying Cu/Zn molar ratio (CZ(x)

@S-*t*). For more details, the CZ(*x*)@S-*t* catalysts with Cu/Zn molar ratios of *x* were prepared as follows: 0.5 g of as-synthesized CZ(*x*)@Si was mixed with 1.25 g of tetrapropyl ammonium hydroxide (TPAOH) (40 wt%) and 2.75 g of DIW solvent, and stirred at room temperature for 10 h to get a well-mixed sol compound. The obtained mixture was further maintained in an oven at 60 °C at a ramping rate of 5 °C min^{-1} for 24 h to obtain dry gels, which were subsequently transferred to 100 mL Teflon-lined autoclaves with 4 mL ammonia solution having a concentration of 28 wt%, sealed, and heated up to 170 °C for successive crystallization durations (*t*) such as 12, 24, 48 or 72 h, respectively. The finally achieved products were washed with DIW several times until the pH value approached ~7 in the upper solution during centrifugation, which was further dried at 80 °C at a ramping rate of 5 °C min^{-1} for 24 h before the calcination treatment at 550 °C at a ramping rate of 1 °C min^{-1} for 2 h under air environment, which was further applied for catalytic activity measurement.

4.2 Evaluation of catalytic activity

Catalytic performance of CZ(*x*)@S-*t* catalysts was evaluated with 0.2 g catalyst in a fixed-bed tubular stainless steel reactor (inner diameter of 6 mm, reactor length of 453 mm). The catalyst was initially activated at 300 °C at a ramp rate of 5 °C min^{-1} for 2 h under a flow of 5 vol% H$_2$ balanced with N$_2$. The CO$_2$ hydrogenation reaction was carried out by using a mixed gas having a molar ratio of CO$_2$/H$_2$/N$_2$ = 24/72/4, where an inert N$_2$ gas for the reaction was used as an internal standard gas to evaluate relative changes of CO$_2$/N$_2$ peak area ratio before and after reaction for CO$_2$ conversion calculation by using eqn (1) as follows. The mixture gas was fed into the reactor maintaining a constant pressure of 5.0 MPa and the reaction temperature was elevated up to 250 °C. Besides, the effluent gases from the reactor were analyzed through an online gas chromatograph (GC, YL6100 from Younglin Co.) equipped with a thermal conductivity detector (TCD) to analyze CO$_2$, CO, N$_2$ and CH$_4$, as well as a flame ionization detector (FID) connected to a Carboxen-1000 packed column and HP-PLOT-U capillary column to analyze organic products such as CH$_4$ and oxygenates (CH$_3$OH and DME), respectively. The X_{CO_2} and S_j (j = CO, CH$_4$, methanol and DME) represent CO$_2$ conversion and selectivity of product j (j = CO, CH$_4$, methanol and DME) in percentage, whereas $N_{CO_2,in}$, $N_{CO_2,out}$ and N_j represent the amount of CO$_2$ feeding, outlet CO$_2$ and formed product j in moles.

$$X_{CO_2} = (N_{CO_2,in} - N_{CO_2,out})/N_{CO_2,in} \times 100\% \quad (1)$$

$$S_j = (N_j/(N_{CO_2,in} - N_{CO_2,out})) \times 100\% \quad (2)$$

4.3 Catalyst characterization

The structural properties of the fresh CZ(*x*)@S-*t* catalysts, including the specific surface area (S_g, m^2 g^{-1}), pore volume

(P_V, cm^3 g^{-1}), and average pore diameter (P_D, nm), were determined by N$_2$ adsorption–desorption analysis at liquid nitrogen temperature of −196 °C using a Micromeritics TRISTAR-3000 instrument. The specific surface area was calculated by using the Brunauer–Emmett–Teller (BET) equation from data in the relative pressure (P/P_0) range of 0.03–0.20. The average pore diameter and pore size distribution were derived from the desorption branch of the isotherms using the Barrett–Joyner–Halenda (BJH) method. Powder X-ray diffraction (XRD) patterns were recorded over the range of 2θ = 5–90° by using a Malvern Panalytical X'Pert PRO MPD diffractometer with Cu Kα radiation to identify crystalline phases of the Cu–ZnO nanoparticles and silicalite-1 zeolite. Particle size distributions and elemental compositions of the CZ(*x*)@S-*t* catalysts were characterized by using scanning-transmission electron microscopy (STEM/TEM) and energy-dispersive X-ray spectroscopy (EDS) with a JEM-F200/JEM-2100F instrument operating at 200 kV. Solid-state magic angle spinning nuclear magnetic resonance (MAS NMR) spectra of ^{29}Si species were acquired on a Varian Unity INOVA 500 MHz NMR spectrometer at a resonance frequency of 130.3 MHz, using a MAS probe spinning at 10 kHz.

The reduction behaviors of the fresh CZ(*x*)@S-*t* catalysts were investigated by temperature-programmed reduction of hydrogen (H$_2$-TPR) using a BELCAT-M instrument. Approximately 50 mg of catalyst was pretreated under a flow of Ar (30 mL min^{-1}) at 300 °C for 1 h at a ramp rate of 10 °C min^{-1}. After cooling to 50 °C, the gas was switched to 5 vol% H$_2$/Ar mixture (30 mL min^{-1}). Reduction profiles were recorded using a thermal conductivity detector (TCD) after passing the effluent gases through a water trap in a temperature range of 100–500 °C to quantify H$_2$ consumption (mmol g$_{cat.}^{-1}$). The surface acidic properties of the fresh CZ(*x*)@S-*t* catalysts were evaluated by temperature-programmed desorption of ammonia (NH$_3$-TPD) using a BELCAT-M instrument. The sample was pretreated under a flow of He at 500 °C for 1 h, cooled down to 100 °C, saturated with NH$_3$ probe gas, and then heated to 800 °C at a ramping rate of 10 °C min^{-1} under He flow to monitor its desorption profiles for NH$_3$ probe molecules. Temperature-programmed desorption of carbon dioxide (CO$_2$-TPD) was similarly performed with ~50 mg of the *in situ* reduced sample at 300 °C for 1 h, which was purged with He flow for 1 h, exposed to CO$_2$ at 50 °C for 1 h, and then heated up to 800 °C at a ramping rate of 10 °C min^{-1} under a flow of He to obtain the desorption profiles of CO$_2$ probe molecules.

In situ diffuse reflectance infrared Fourier transform spectroscopy (DRIFTS) analysis was conducted by using a PerkinElmer Frontier FT-IR spectrometer equipped with a PIKE Technologies diffuse reflection cell with a resolution of 4 cm^{-1}. Approximately 20 mg of the fresh CZ(*x*)@S-*t* catalyst was loaded into a DRIFT cell, reduced under a flow of 5 vol% H$_2$/N$_2$ at 300 °C for 1 h, purged with N$_2$ for 2 h, and cooled to ambient temperature to acquire reference background spectra. The reactant gas mixture (CO$_2$/H$_2$/N$_2$ = 24/72/4 vol%) was then introduced at the pressure of 2.0 MPa while heating

to 300 °C and holding for 2 h. Temperature-resolved spectra were collected every 10 °C during the heating step, and time-resolved spectra were recorded 5-minute interval at 300 °C for 2 h to identify the adsorbed surface intermediates. Furthermore, *in situ* CO-DRIFTS analysis was carried out to verify oxidation states of metallic Cu species during the CO_2-to-DME reaction. Approximately 20 mg catalyst was reduced at 300 °C under 5 vol% H_2/N_2 flow (15 mL min^{-1}) for 2 h and cooled to 30 °C. The flow was switched to inert N_2 (99.99%), followed by H_2 flow (100 mL min^{-1}) for 30 minutes to reduce partially oxidized surfaces under air exposure. Subsequently, CO (99.99%, 30 mL min^{-1}) was introduced at 30 °C for 30 minutes, and after purging with inert N_2 flow for additional 30 minutes, CO-DRIFT spectra were collected at a fixed temperature of 30 °C.

Author contributions

Jong Wook Bae, Eunjoo Jang, and Xu Wang conceived and designed the idea as well as revised the manuscript. Xu Wang and Chundong Zhang performed the catalytic reactions, conducted the characterization and related experiments and wrote the manuscript. Dongming Shen, Hui Kang, Kangzhou Wang, Xinhua Gao, and Jianli Zhang analyzed and interpreted all the data from characterization and catalytic performances.

Conflicts of interest

We all declare no financial/commercial conflicts of interest.

Data availability

Supplementary information is available. See DOI: **https://doi.org/10.1039/D5IM00166H**.

The data supporting this article have been included as part of the SI.

Acknowledgements

References

1 J. Ye, N. Dimitratos, L. M. Rossi, N. Thonemann, A. M. Beale and R. Wojcieszak, Hydrogenation of CO_2 for sustainable fuel and chemical production, *Science*, 2025, **387**, eadn9388.

2 R. Ye, J. Ding, T. R. Reina, M. S. Duyar, H. Li, W. Luo, R. Zhang, M. Fan, G. Feng, J. Sun and J. Liu, Design of catalysts for selective CO_2 hydrogenation, *Nat. Synth.*, 2025, **4**, 288–302.

3 R. P. Ye, J. Ding, W. Gong, D. A. Morris, Q. Zhang, Y. Wang, C. K. Russell, Z. Xu, A. G. Russell, Q. Li, M. Fan and Y.-G. Yao, CO_2 hydrogenation to high-value products via heterogeneous catalysis, *Nat. Commun.*, 2019, **10**, 5698.

4 Y. Ni, J. Tian, Z. Han, Y. Chai, C. Zhao, G. Wu and L. Li, Catalysis in sustainable energy resources: Overview studies of hydrogen, methane, biomass and plastics, *Ind. Chem. Mater.*, 2025, **3**, 257–276.

5 A. Álvarez, A. Bansode, A. Urakawa, A. V. Bavykina, T. A. Wezendonk, M. Makkee, J. Gascon and F. Kapteijn, Challenges in the greener production of formates/formic acid, methanol, and DME by heterogeneously catalyzed CO_2 hydrogenation processes, *Chem. Rev.*, 2017, **117**, 9804–9838.

6 K. Saravanan, H. Ham, N. Tsubaki and J. W. Bae, Recent progress for direct synthesis of dimethyl ether from syngas on the heterogeneous bifunctional hybrid catalysts, *Appl. Catal., B*, 2017, **217**, 494–522.

7 K. B. Tan, K. Xu, D. Cai, J. Huang and G. Zhan, Rational design of bifunctional catalysts with proper integration manners for CO and CO_2 hydrogenation into value-added products: A review, *Chem. Eng. J.*, 2023, **463**, 142262.

8 X. Jiang, X. Nie, X. Guo, C. Song and J. G. Chen, Recent advances in carbon dioxide hydrogenation to methanol via heterogeneous catalysis, *Chem. Rev.*, 2020, **120**, 7984–8034.

9 X. Cui, W. Yan, H. Yang, Y. Shi, Y. Xue, H. Zhang, Y. Niu, W. Fan and T. Deng, Preserving the active Cu–ZnO interface for selective hydrogenation of CO_2 to dimethyl ether and methanol, *ACS Sustainable Chem. Eng.*, 2021, **9**, 2661–2672.

10 B. Liang, J. Ma, X. Su, C. Yang, H. Duan, H. Zhou, S. Deng, L. Li and Y. Huang, Investigation on deactivation of Cu/ZnO/Al_2O_3 catalyst for CO_2 hydrogenation to methanol, *Ind. Eng. Chem. Res.*, 2019, **58**, 9030–9037.

11 A. Prašnikar, A. Pavlišič, F. Ruiz-Zepeda, J. Kovač and B. Likozar, Mechanisms of copper-based catalyst deactivation during CO_2 reduction to methanol, *Ind. Eng. Chem. Res.*, 2019, **58**, 13021–13029.

12 W. Wu, Y. Wang, L. Luo, M. Wang, Z. Li, Y. Chen, Z. Wang, J. Chai, Z. Cen, Y. Shi, J. Zhao, J. Zeng and H. Li, CO_2 Hydrogenation over copper/ZnO single-atom catalysts: Water-promoted transient synthesis of methanol, *Angew. Chem., Int. Ed.*, 2022, **61**, e202213024.

13 M. Kosari, U. Anjum, S. Xi, A. M. H. Lim, A. M. Seayad, E. A. J. Raj, S. M. Kozlov, A. Borgna and H. C. Zeng, Revamping SiO_2 spheres by core–shell porosity endowment to construct a mazelike nanoreactor for enhanced catalysis in CO_2 hydrogenation to methanol, *Adv. Funct. Mater.*, 2021, **31**, 2102896.

14 J. Zhong, X. Yang, Z. Wu, B. Liang, Y. Huang and T. Zhang, State of the art and perspectives in heterogeneous catalysis of CO_2 hydrogenation to methanol, *Chem. Soc. Rev.*, 2020, **49**, 1385–1413.

15 T. P. Araújo, S. Mitchell and J. Pérez-Ramírez, Design principles of catalytic materials for CO_2 hydrogenation to methanol, *Adv. Mater.*, 2024, **36**, 2409322.

16 E. L. Kunkes, F. Studt, F. Abild-Pedersen, R. Schlögl and M. Behrens, Hydrogenation of CO_2 to methanol and CO on Cu/ZnO/Al_2O_3: Is there a common intermediate or not?, *J. Catal.*, 2015, **328**, 43–48.

17 M. Liu, C. Miao and Z. Wu, Recent advances in the synthesis, characterization, and catalytic consequence of metal species confined within zeolite for hydrogen-related reactions, *Ind. Chem. Mater.*, 2024, **2**, 57–84.

18 W. G. Cui, Y. T. Li, L. Yu, H. Zhang and T. L. Hu, Zeolite-encapsulated ultrasmall Cu/ZnOx nanoparticles for the hydrogenation of CO_2 to methanol, *ACS Appl. Mater. Interfaces*, 2021, **13**, 18693–18703.

19 Y. Li, T. Du, C. Chen, H. Jia, J. Sun, X. Fang, Y. Wang and H. Na, Copper nanoparticles encapsulated in zeolite 13X for highly selective hydrogenation of CO_2 to methanol, *J. Environ. Chem. Eng.*, 2024, **12**, 111856.

20 R. Kanomata, K. Awano, H. Fujitsuka, K. Kimura, S. Yasuda, R. Simancas, S. Bekhti, T. Wakihara, T. Yokoi and T. Tago, Development of silicalite-1 encapsulated Cu-ZnO catalysts for methanol synthesis by CO_2 hydrogenation, *Chem. Eng. J.*, 2024, **485**, 149896.

21 Y. Chai, B. Qin, B. Li, W. Dai, G. Wu, N. Guan and L. Li, Zeolite-encaged mononuclear copper centers catalyze CO_2 selective hydrogenation to methanol, *Natl. Sci. Rev.*, 2023, **10**, nwad043.

22 X. Meng, C. Wang, S. Chae, Y. Wang, C. Wu, S. Xi, E. Catizzone, G. Giordano, H. Guo and S. Mintova, CuZnOx active sites anchored on the silanols of hollow silicalite-1 zeolite enhance CO_2 hydrogenation to methanol, *ACS Catal.*, 2025, **15**, 5412–5425.

23 U. J. Etim, Y. Chen and Z. Zhong, Cu nanoparticles immobilized in mesopores generated in zeolite for high-performing CO_2 hydrogenation to methanol, *Chem. Eng. J.*, 2024, **498**, 155783.

24 X. Wang, H. Y. Woo, D. Shen, M. J. Park, M. Ali, F. Zafar, K. Y. Kang, J. S. Choi, E. Jang and J. W. Bae, Cu–ZnO nanoparticles encapsulated in ZSM-5 for selective conversion of carbon dioxide into oxygenates, *EES Catal.*, 2025, **3**, 420–434.

25 G. Liu, J. Liu, N. He, C. Miao, J. Wang, Q. Xin and H. Guo, Silicalite-1 zeolite acidification by zinc modification and its catalytic properties for isobutane conversion, *RSC Adv.*, 2018, **8**, 18663–18671.

26 X. Xue, J. Tao, Y. Jia, T. Bai, W. Huang, S. Guo, Y. Zhang, Y. Zhou and Q. Wei, In situ synthesis of Zn/silicalite-1 via subcrystals: Constructing a framework with abundant weak acid sites and high stability, *J. Phys. Chem. C*, 2025, **129**, 6719–6727.

27 J. Huang, J. Zhang, S. Lu, Y. Liang and F. S. Xiao, Pure silica Beta zeolite supported copper species for efficient hydrogenolysis of glycerol to 1,2-propanediol, *Biomass Bioenergy*, 2023, **174**, 106818.

28 C. H. Cheng and D. F. Shantz, Silicalite-1 growth from clear solution: Effect of the structure-directing agent on growth kinetics, *J. Phys. Chem. B*, 2005, **109**, 13912–13920.

29 W. O. Parker and R. Millini, Ti coordination in titanium silicalite-1, *J. Am. Chem. Soc.*, 2006, **128**, 1450–1451.

30 T. Guo, B. Wang, C. Xue, X. Liu, C. Lin, X. Xie, Y. Luo, W. Liao and X. Shu, In situ tailoring the crystalline defects of titanium silicalite-1 (TS-1) to improve the 1-butene epoxidation performance, *Ind. Eng. Chem. Res.*, 2024, **63**, 11872–11880.

31 F. Yi, F. Chen, Z. Tao, C. Hu, X. Yi, A. Zheng, X. Wen, Y. Yun, Y. Yang and Y. Li, Origin of weak Lewis acids on silanol nests in dealuminated zeolite Beta, *J. Catal.*, 2019, **380**, 204–214.

32 M. Orazov and M. E. Davis, Catalysis by framework zinc in silica-based molecular sieves, *Chem. Sci.*, 2016, **7**, 2264–2274.

33 F. Yaripour, F. Baghaei, I. Schmidt and J. Perregaard, Catalytic dehydration of methanol to dimethyl ether (DME) over solid-acid catalysts, *Catal. Commun.*, 2005, **6**, 147–152.

34 B. Ma, H. Pan, F. Yang, X. Liu, Y. Guo and Y. Wang, Efficient CO_2 catalytic hydrogenation over CuOx–ZnO/silicalite-1 with stable Cu^+ species, *Catal. Sci. Technol.*, 2022, **12**, 5850–5860.

35 S. Zhang, J. Ye, J. Shen, Y. Guo, W. Zhan, L. Wang, X. Tang, S. Dai and Y. Guo, Direct oxidation of methane to C1 oxygenates on Cu/ZSM-5: Reaction property and configuration of Cu species, *ChemCatChem*, 2024, **16**, e202401137.

36 H. Wang, J. Jia, S. Liu, H. Chen, Y. Wei, Z. Wang, L. Zheng, Z. Wang and R. Zhang, Highly efficient NO abatement over Cu-ZSM-5 with special nanosheet features, *Environ. Sci. Technol.*, 2021, **55**, 5422–5434.

37 Y. Zhang, D. Li, Y. Zhang, Y. Cao, S. Zhang, K. Wang, F. Ding and J. Wu, V-modified CuO–ZnO–ZrO_2/HZSM-5 catalyst for efficient direct synthesis of DME from CO_2 hydrogenation, *Catal. Commun.*, 2014, **55**, 49–52.

38 R. Singh, K. Tripathi, K. K. Pant and J. K. Parikh, Unravelling synergetic interaction over tandem Cu-ZnO-ZrO_2/hierarchical ZSM5 catalyst for CO_2 hydrogenation to methanol and DME, *Fuel*, 2022, **318**, 123641.

39 C. Huang, J. Wen, Y. Sun, M. Zhang, Y. Bao, Y. Zhang, L. Liang, M. Fu, J. Wu, D. Ye and L. Chen, CO_2 hydrogenation to methanol over Cu/ZnO plate model catalyst: Effects of reducing gas induced Cu nanoparticle morphology, *Chem. Eng. J.*, 2019, **374**, 221–230.

40 K. Hadjiivanov and H. Knözinger, FTIR study of low-temperature CO adsorption on Cu-ZSM-5: Evidence of the formation of $Cu^{2+}(CO)_2$ species, *J. Catal.*, 2000, **191**, 480–485.

41 C. Huang, Y. Chen, H. Fang, G. Zhi, C. Chen, Y. Luo, X. Lin and L. Jiang, Copper phyllosilicate-derived Cu catalyst for the water–gas shift reaction: Insight into the role of Cu^+–Cu^0 and reaction mechanism, *ACS Catal.*, 2025, **15**, 5546–5556.

42 L. Yao, X. Shen, Y. Pan and Z. Peng, Synergy between active sites of Cu-In-Zr-O catalyst in CO_2 hydrogenation to methanol, *J. Catal.*, 2019, **372**, 74–85.

43 T. Kristiansen and K. Mathisen, On the promoting effect of water during NO_x removal over single-site copper in hydrophobic silica APD-aerogels, *J. Phys. Chem. C*, 2014, **118**, 2439–2453.

44 Z. Qu, Y. Li, S. Huang, P. Chen and X. Ma, Clarification of copper species over Cu-SAPO-34 catalyst by DRIFTS and DFT study of CO adsorption, *Sci. China:Chem.*, 2017, **60**, 912–919.

45 J. H. Kwak, T. Varga, C. H. F. Peden, F. Gao, J. C. Hanson and J. Szanyi, Following the movement of Cu ions in a SSZ-13 zeolite during dehydration, reduction and adsorption: A combined in situ TP-XRD, XANES/DRIFTS study, *J. Catal.*, 2014, **314**, 83–93.

46 J. Yu, M. Yang, J. Zhang, Q. Ge, A. Zimina, T. Pruessmann, L. Zheng, J. D. Grunwaldt and J. Sun, Stabilizing Cu^+ in Cu/SiO_2 catalysts with a shattuckite-like structure boosts CO_2 hydrogenation into methanol, *ACS Catal.*, 2020, **10**, 14694–14706.

47 P. Sripada, J. Kimpton, A. Barlow, T. Williams, S. Kandasamy and S. Bhattacharya, Investigating the dynamic structural changes on Cu/CeO_2 catalysts observed during CO_2 hydrogenation, *J. Catal.*, 2020, **381**, 415–426.

48 B. Yang, W. Deng, L. Guo and T. Ishihara, Copper-ceria solid solution with improved catalytic activity for hydrogenation of CO_2 to CH_3OH, *Chin. J. Catal.*, 2020, **41**, 1348–1359.

49 W. Wang, Z. Qu, L. Song and Q. Fu, Probing into the multifunctional role of copper species and reaction pathway on copper-cerium-zirconium catalysts for CO_2 hydrogenation to methanol using high pressure in situ DRIFTS, *J. Catal.*, 2020, **382**, 129–140.

50 A. Atakan, E. Erdtman, P. Mäkie, L. Ojamäe and M. Odén, Time evolution of the CO_2 hydrogenation to fuels over Cu-Zr-SBA-15 catalysts, *J. Catal.*, 2018, **362**, 55–64.

51 V. K. Velisoju, J. L. Cerrillo, R. Ahmad, H. O. Mohamed, Y. Attada, Q. Cheng, X. Yao, L. Zheng, O. Shekhah, S. Telalovic, J. Narciso, L. Cavallo, Y. Han, M. Eddaoudi, E. V. Ramos-Fernández and P. Castaño, Copper nanoparticles encapsulated in zeolitic imidazolate framework-8 as a stable and selective CO_2 hydrogenation catalyst, *Nat. Commun.*, 2024, **15**, 2045.

52 P. Wu and B. Yang, Significance of surface formate coverage on the reaction kinetics of methanol synthesis from CO_2 hydrogenation over Cu, *ACS Catal.*, 2017, **7**, 7187–7195.

53 M. Bowker, R. A. Hadden, H. Houghton, J. N. K. Hyland and K. C. Waugh, The mechanism of methanol synthesis on copper/zinc oxide/alumina catalysts, *J. Catal.*, 1988, **109**, 263–273.